

Solvent-free coarse-grained lipid model for large-scale simulations

Hiroshi Noguchi*

Institute for Solid State Physics, University of Tokyo, Kashiwa, Chiba 277-8581, Japan

(Dated: October 23, 2018)

A coarse-grained molecular model, which consists of a spherical particle and an orientation vector, is proposed to simulate lipid membrane on a large length scale. The solvent is implicitly represented by an effective attractive interaction between particles. A bilayer structure is formed by orientation-dependent (tilt and bending) potentials. In this model, the membrane properties (bending rigidity, line tension of membrane edge, area compression modulus, lateral diffusion coefficient, and flip-flop rate) can be varied over broad ranges. The stability of the bilayer membrane is investigated via droplet-vesicle transition. The rupture of the bilayer and worm-like micelle formation can be induced by an increase in the spontaneous curvature of the monolayer membrane.

PACS numbers:

I. INTRODUCTION

Amphiphilic molecules, such as lipids and detergents, self-assemble into various structures depending on the relative size of their hydrophilic parts: spherical or worm-like micelles, bilayer membranes, inverted hexagonal structures, and inverted micelles. Among these structures, the bilayer membrane of phospholipids has been intensively investigated, since it is the basic structure of the plasma membrane and the intracellular compartments of living cells, where the membranes are in a fluid phase and lipid molecules can diffuse in quasi-two-dimensional space. A vesicle (closed membrane) is considered to be a simple model of cells and it has applications in drug-delivery systems as a drug carrier.

Bilayer membranes exhibit many interesting phenomena such as shape deformation induced by phase separation or chemical reaction, membrane fusion, and membrane fission. The length scale of these phenomena varies from nm to μm , since cells are $\sim 10\mu\text{m}$ in diameter, whereas the thickness of a biomembrane is 5nm. To investigate the morphologies of cells and vesicles, the molecular structure is assumed to be negligible, and the bilayer membrane is described as a smoothly-curved mathematical surface¹⁻³. The information about the bilayer properties is only reflected in the values of the elastic parameters. To simulate the membrane with thermal fluctuations, a triangulated surface is widely used^{4,5}. An alternative model is a meshless membrane⁶⁻¹³, where particles self-assemble into a membrane by anisotropic potential interactions. These models can reproduce μm -scale dynamics of the bilayer membrane well but cannot treat a non-bilayer structure such as the stalk structure of a membrane fusion intermediate^{14,15}.

To simulate molecular-scale dynamics and the non-bilayer structure, a molecular model is required. Although computer technology has grown rapidly, the typical scale for recent simulations of the all-atom models is only 100 ns dynamics of hundreds of lipid molecules. To simulate the membranes on longer and larger scales, various coarse-grained molecular models have been proposed (see review articles¹⁶⁻²⁰). Recently, the potential param-

eters in some of the coarse-grained molecular models are tuned by atomistic simulations²¹⁻²⁵. In mapping of interaction parameters, one coarse-grained particle typically represents three or four heavy atoms and their accompanying hydrogen atoms. To further reduce the computational costs, larger segments (three or more segment particles per amphiphilic molecule) are employed, and the solvent is implicitly represented by an effective attractive potential between the hydrophobic segments^{19,26-30}. Model parameters are chosen to generate a bilayer membrane with reasonably realistic values of elastic properties. In this scale, it is difficult to take into account chemical details of lipids, such as an unsaturated bond in hydrocarbon chains. Instead, this type of models can be advantageous to capture the general features in the bilayer membrane, since the simplicity of the model can allow for wide ranges of variation of the membrane properties.

In this paper, we propose a solvent-free molecular model to pursue two purposes: (1) to represent the amphiphilic molecule in a size as small as possible and (2) to allow the variation in the membrane properties for wide ranges. A molecule consisting of many particles has a higher resolution than that with less particles but requires a smaller length unit and time step for simulations. Here, we consider a molecule that consists of a spherical particle and an orientation vector. It can reduce computational costs to simulate many molecules. In previous solvent-free models^{19,25-30}, the membrane properties are varied only in narrow ranges. On the other hand, in one of the meshless membrane models, the bending rigidity and the line tension of the membrane edge can be independently varied over wide ranges⁷. This allows the conditions of vesicle formation and rupture to be controlled⁸. In addition, it is easy to compare the simulation results with theoretical predictions. Such tuning capability is desired for molecular models.

In Sec. II, the lipid model and the simulation method are described. In Sec. III, the results and discussion are provided. The formation of a membrane and its stability for droplet-vesicle transitions are described in Sec. III A. In Sec. III B and III C, the calculation methods

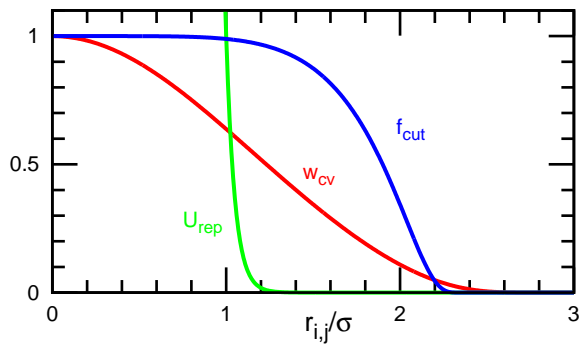


FIG. 1: (Color online) The cutoff function $f_{\text{cut}}(r_{ij})$, the compact Gaussian weight function $w_{\text{cv}}(r_{ij})$, and the repulsive potential $U_{\text{rep}}(r_{ij})$.

and the dependence of the static and dynamic properties on model parameters are described, respectively. The summary is given in Sec. IV.

II. MODEL AND METHOD

A. Molecular model

In solvent-free lipid models, an amphiphilic molecule is typically represented by three or more particles¹⁹. Here, we consider a lipid molecule with minimum (5) degrees of freedom for solvent-free molecular simulations. Each (i -th) molecule has a spherical particle with an orientation vector \mathbf{u}_i , which represents a direction from the hydrophobic to the hydrophilic part. There are two points of interaction in the molecule: the center of a sphere \mathbf{r}_i^s and a hydrophilic point $\mathbf{r}_i^e = \mathbf{r}_i^s + \mathbf{u}_i$. The molecules interact with each other via the potential,

$$\begin{aligned} \frac{U}{k_B T} = & \sum_{i < j} U_{\text{rep}}(r_{i,j}^s) + \varepsilon \sum_i U_{\text{att}}(\rho_i) \quad (1) \\ & + \frac{k_{\text{tilt}}}{2} \sum_{i < j} \left[(\mathbf{u}_i \cdot \hat{\mathbf{r}}_{ij}^s)^2 + (\mathbf{u}_j \cdot \hat{\mathbf{r}}_{ij}^s)^2 \right] w_{\text{cv}}(r_{ij}^e) \\ & + \frac{k_{\text{bend}}}{2} \sum_{i < j} \left(\mathbf{u}_i - \mathbf{u}_j - C_{\text{bd}} \hat{\mathbf{r}}_{ij}^s \right)^2 w_{\text{cv}}(r_{ij}^e), \end{aligned}$$

where $\mathbf{r}_{i,j} = \mathbf{r}_i - \mathbf{r}_j$, $r_{i,j} = |\mathbf{r}_{i,j}|$, $\hat{\mathbf{r}}_{i,j} = \mathbf{r}_{i,j}/r_{i,j}$, and $k_B T$ is the thermal energy. The molecules have an excluded volume with a diameter σ via the repulsive potential,

$$U_{\text{rep}}(r) = \exp[-20(r/\sigma - 1)], \quad (2)$$

with a cutoff at $r = 2.4\sigma$.

The second term in Eq. (1) represents the attractive interaction between the molecules. A multibody attractive potential $U_{\text{att}}(\rho_i)$ is employed to mimic the ‘‘hydrophobic’’ interaction. This potential allows the formation of the fluid membrane over wide parameter ranges

and fast lateral diffusion. Similar potentials have been applied in the previous membrane models^{7,26,30} and a coarse-grained protein model³¹. The potential $U_{\text{att}}(\rho_i)$ is given by

$$U_{\text{att}}(\rho_i) = 0.25 \ln[1 + \exp\{-4(\rho_i - \rho^*)\}] - C, \quad (3)$$

where $C = 0.25 \ln\{1 + \exp(4\rho^*)\} \simeq \rho^*$ is chosen such that $U_{\text{att}}(0) = 0$. The local particle density ρ_i is approximately the number of particles \mathbf{r}_i^s in the sphere whose radius is r_{att} .

$$\rho_i = \sum_{j \neq i} f_{\text{cut}}(r_{i,j}^s), \quad (4)$$

where $f_{\text{cut}}(r)$ is a C^∞ cutoff function,

$$f_{\text{cut}}(r) = \begin{cases} \exp\{A(1 + \frac{1}{(r/r_{\text{cut}})^n - 1})\} & (r < r_{\text{cut}}) \\ 0 & (r \geq r_{\text{cut}}) \end{cases} \quad (5)$$

with $n = 6$, $A = \ln(2)\{(r_{\text{cut}}/r_{\text{att}})^n - 1\}$, $r_{\text{att}} = 1.9\sigma$ ($f_{\text{cut}}(r_{\text{att}}) = 0.5$), and the cutoff radius $r_{\text{cut}} = 2.4\sigma$ (see Fig. 1). The potential $U_{\text{att}}(\rho_i)$ acts as a pairwise attractive potential ($U_{\text{att}}(\rho_i) \simeq \rho$, so that $\sum_i U_{\text{att}}(\rho_i) \simeq -2 \sum_{i < j} f_{\text{cut}}(r_{i,j}^s)$) for $\rho_i < \rho^* - 1$ and approaches a constant value ($U_{\text{att}}(\rho_i) \simeq \rho^*$) for $\rho_i > \rho^* + 1$. It is assumed that the hydrophobic parts have no contact with the implicit solvent (void space) at $\rho_i \gtrsim \rho^*$.

The third and fourth terms in Eq. (1) are discretized versions of tilt and bending potentials of the tilt model^{32,33}, respectively. A smoothly truncated Gaussian function⁷ is employed as a weight function

$$w_{\text{cv}}(r) = \begin{cases} \exp(\frac{(r/r_{\text{ga}})^2}{(r/r_{\text{cc}})^n - 1}) & (r < r_{\text{cc}}) \\ 0 & (r \geq r_{\text{cc}}) \end{cases} \quad (6)$$

with $n = 4$, $r_{\text{ga}} = 1.5\sigma$, and $r_{\text{cc}} = 3\sigma$ (see Fig. 1). All orders of derivatives of $f_{\text{cut}}(r)$ and $w_{\text{mfs}}(r)$ are continuous at the cutoff radii. The weight is a function of r_{ij}^e (not r_{ij}^s) to avoid the interaction between the molecules in the opposite monolayers of the bilayer. The average distance between the neighboring molecules in the same monolayer is $\bar{r}_{\text{nb}} \simeq 1.05\sigma$, and the distance to the neighboring molecule in the other monolayer is $r_{ij}^e \simeq 3\sigma$ (see Fig. 2(a)). Thus, these two potentials act between the neighboring molecules in the same monolayer but not between the monolayers. The tilt potential has the energy minimum in a completely flat membrane with no tilt deformation. Similar tilt potentials have been used in the meshless membrane models^{6,9-13}. The same type of bending potential [the fourth term in Eq. (1)] was previously used to control the bending rigidity and the spontaneous curvature of the monolayer in the molecular simulations^{27,30}. Positive spontaneous curvature indicates that the hydrophilic head is larger than the hydrophobic tail of amphiphilic molecules. The bending rigidity is numerically calculated and compared with the estimation from the continuous description of the membrane in Sec. III C.

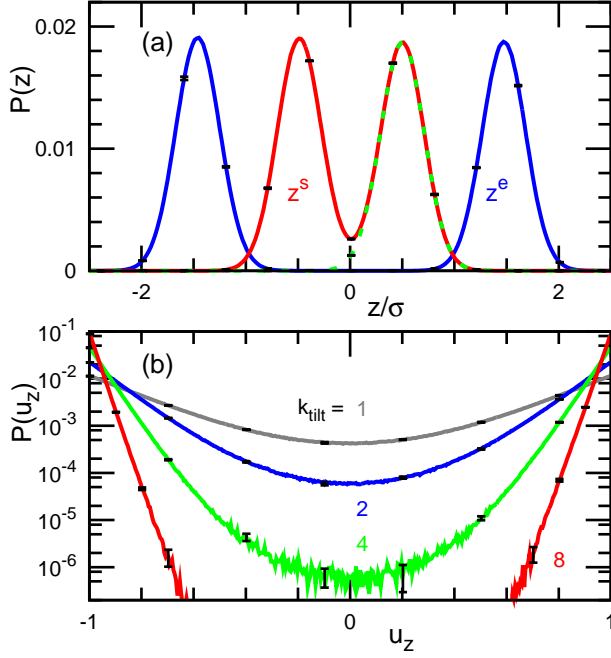


FIG. 2: (Color online) Probability distribution of (a) the positions and (b) the orientation of the molecules in the planar membrane at $N = 512$, $\rho^* = 14$, $\varepsilon = 2$, $k_{\text{bend}} = k_{\text{tilt}}$, and $C_{\text{bd}} = 0$. (a) The z components of \mathbf{r}_i^s and \mathbf{r}_i^e are shown for $k_{\text{tilt}} = 8$. The dashed line represents \mathbf{r}_i^s of the molecules at $u_z > 0$. (b) The z component u_z of the molecular orientation is shown for $k_{\text{tilt}} = 1, 2, 4$, and 8 . The error bars are displayed at several data points.

B. Brownian dynamics

We simulated the membrane in the NVT ensemble (constant number of molecules N , volume V , and temperature T) with periodic boundary conditions in a box with side length L_x , L_y , and L_z . We employed Brownian dynamics (molecular dynamics with Langevin thermostat). The motions of the center of the mass $\mathbf{r}_i^G = (\mathbf{r}_i^s + \mathbf{r}_i^e)/2$ and the orientation \mathbf{u}_i are given by underdamped Langevin equations:

$$\frac{d\mathbf{r}_i^G}{dt} = \mathbf{v}_i^G, \quad \frac{d\mathbf{u}_i}{dt} = \boldsymbol{\omega}_i, \quad (7)$$

$$m \frac{d\mathbf{v}_i^G}{dt} = -\zeta_G \mathbf{v}_i^G + \mathbf{g}_i^G(t) + \mathbf{f}_i^G, \quad (8)$$

$$I \frac{d\boldsymbol{\omega}_i}{dt} = -\zeta_r \boldsymbol{\omega}_i + (\mathbf{g}_i^r(t) + \mathbf{f}_i^r)^\perp + \lambda \mathbf{u}_i, \quad (9)$$

where m and I are the mass and the moment of inertia of the molecule, respectively. The forces are given by $\mathbf{f}_i^G = -\partial U/\partial \mathbf{r}_i^G$ and $\mathbf{f}_i^r = -\partial U/\partial \mathbf{u}_i$ with the perpendicular component $\mathbf{a}^\perp = \mathbf{a} - (\mathbf{a} \cdot \mathbf{u}_i)\mathbf{u}_i$ and a Lagrange multiplier λ to keep $\mathbf{u}_i^2 = 1$. According to the fluctuation-dissipation theorem, the friction coefficients ζ_G , ζ_r and the Gaussian white noises $\mathbf{g}_i^G(t)$, $\mathbf{g}_i^r(t)$ obey the following relations: the average $\langle g_{i,\alpha_1}^{\beta_1}(t) \rangle = 0$ and the variance

$\langle g_{i,\alpha_1}^{\beta_1}(t) g_{j,\alpha_2}^{\beta_2}(t') \rangle = 2k_B T \zeta_{\beta_1} \delta_{ij} \delta_{\alpha_1 \alpha_2} \delta_{\beta_1 \beta_2} \delta(t - t')$, where $\alpha_1, \alpha_2 \in \{x, y, z\}$ and $\beta_1, \beta_2 \in \{G, r\}$. The Langevin equations are integrated by the leapfrog algorithm³⁴ with $\mathbf{v}_{i,n} \equiv \mathbf{v}_i(t_n) = (\mathbf{v}_i(t_{n+1/2}) + \mathbf{v}_i(t_{n-1/2}))/2$. First, the velocities are updated by

$$\mathbf{v}_{i,n+1/2}^G = a_0 \mathbf{v}_{i,n-1/2}^G + a_1 (\mathbf{g}_{i,n}^G + \mathbf{f}_{i,n}^G), \quad (10)$$

$$\boldsymbol{\omega}'_{i,n+1/2} = b_0 \boldsymbol{\omega}_{i,n-1/2} + b_1 (\mathbf{g}_{i,n}^r + \mathbf{f}_{i,n}^r)^\perp + \lambda' \mathbf{u}_{i,n},$$

$$\mathbf{u}'_{i,n+1/2} = \mathbf{u}_{i,n} + \boldsymbol{\omega}'_{i,n+1/2} \Delta t / 2,$$

$$\boldsymbol{\omega}_{i,n+1/2} = \boldsymbol{\omega}'_{i,n+1/2} - (\boldsymbol{\omega}'_{i,n+1/2} \cdot \mathbf{u}'_{i,n+1/2}) \mathbf{u}'_{i,n+1/2},$$

where

$$a_0 = \frac{1 - \zeta_G \Delta t / 2m}{1 + \zeta_G \Delta t / 2m}, \quad a_1 = \frac{\Delta t / m}{1 + \zeta_G \Delta t / 2m}, \quad (11)$$

$$b_0 = \frac{1 - \zeta_r \Delta t / 2I}{1 + \zeta_r \Delta t / 2I}, \quad b_1 = \frac{\Delta t / I}{1 + \zeta_r \Delta t / 2I},$$

$$\lambda' = \lambda \Delta t / I = -\frac{2\boldsymbol{\omega}_{i,n-1/2} \cdot \mathbf{u}_{i,n}}{1 + \zeta_r \Delta t / 2I},$$

$$\mathbf{g}_{i,n}^{\beta_1} = \mathbf{g}_i^{\beta_1}(t_n) / \sqrt{\Delta t}.$$

Then, the positions are updated by

$$\mathbf{r}_{i,n+1}^G = \mathbf{r}_{i,n}^G + \mathbf{v}_{i,n+1/2}^G \Delta t, \quad (12)$$

$$\mathbf{u}'_{i,n+1} = \mathbf{u}_{i,n} + \boldsymbol{\omega}_{i,n+1/2} \Delta t,$$

$$\mathbf{u}_{i,n+1} = \mathbf{u}'_{i,n+1} / |\mathbf{u}'_{i,n+1}|.$$

We employed $m = 1$, $I = 1$, $\zeta_G = 1$, $\zeta_r = 1$, $k_B T = 1$, $\Delta t = 0.005$, and the total number of the molecules $N = 300$ to 8192 . The results are displayed with the length unit σ , the energy unit $k_B T$, and the time unit $\tau_0 = \zeta_G \sigma^2 / k_B T$. The diffusion coefficient D is normalized using the diffusion coefficient $D_0 = \sigma^2 / \tau_0$ of an isolated molecule. The error bars of the data are estimated from the standard deviations of three to six independent runs.

III. RESULTS AND DISCUSSION

A. Self-assembly and membrane stability

Molecules self-assemble into spherical droplets at $k_{\text{bend}} = k_{\text{tilt}} = 0$, i.e., when only the first two terms in Eq. (1) are taken into account. When the third term (the tilt potential) is added, the molecules can spontaneously form vesicles. Figure 3 shows the self-assembly of molecules from a random gas state. First, small clusters are formed; these clusters merge into disk-like micelles. Then, a large disk closes into a vesicle through a bowl-like shape (see Fig. 3(c)). Similar self-assembly processes have been observed in the previous simulations of molecular²⁶ and meshless⁸ models.

In order to clarify the stability of three-dimensional aggregates and bilayer membranes, the morphologies of the aggregates are investigated as k_{tilt} gradually increases or decreases. As k_{tilt} increases, a spherical liquid droplet

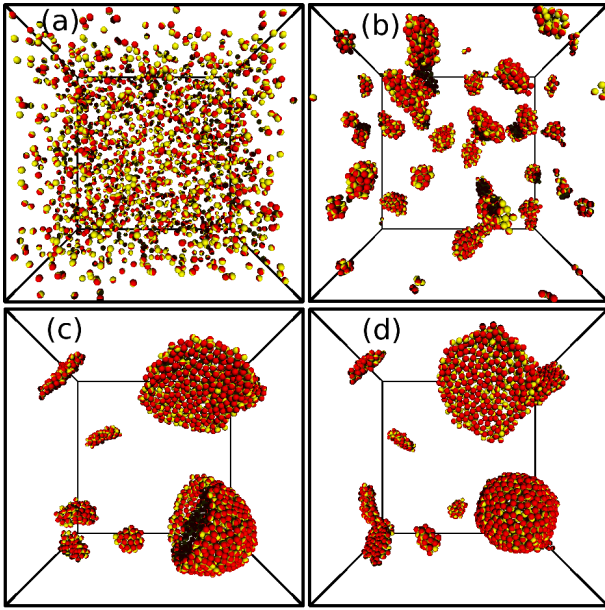


FIG. 3: (Color online) Sequential snapshots of the molecular self-assembly at $N = 2000$, $L_x = L_y = L_z = 40\sigma$, $\varepsilon = 2$, $\rho^* = 14$, $k_{\text{bend}} = 0$, $k_{\text{tilt}} = 8$, and $C_{\text{bd}} = 0$. (a) $t/\tau_0 = 0$. (b) $t/\tau_0 = 500$. (c) $t/\tau_0 = 16650$. (d) $t/\tau_0 = 16700$.

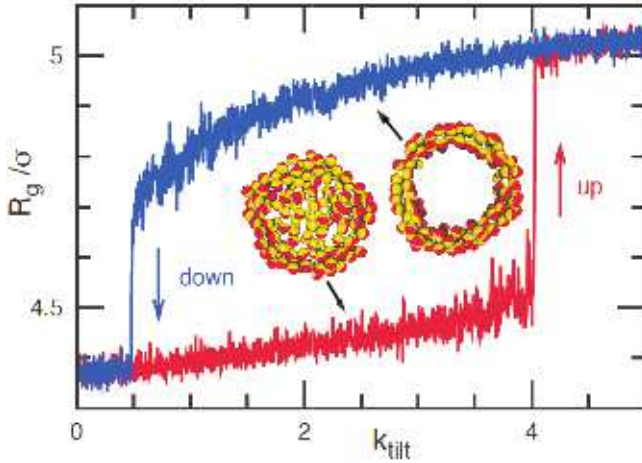


FIG. 4: (Color online) Droplet-vesicle transition at $N = 500$, $\varepsilon = 2$, $\rho^* = 14$, $k_{\text{bend}} = 4$, and $C_{\text{bd}} = 0$. The lower and upper lines represent the radius of gyration R_g in k_{tilt} increasing or decreasing, respectively. Sliced snapshots are also shown at $k_{\text{tilt}} = 2.5$.

transforms into a bilayer vesicle. At the transition point ($k_{\text{tilt}} = 4$), the radius of gyration R_g exhibits an abrupt increase as shown in Fig. 4. As k_{tilt} decreases, the transition from a vesicle to a droplet occurs, however, the transition point ($k_{\text{tilt}} = 0.5$) is much lower. Thus, a typical hysteresis for the first-order transition is observed. The rate of increase or decrease is sufficiently low ($k_{\text{tilt}} = 0.0005t/\tau_0$). We checked that the deviation of the transition points by the annealing rates is very small; $\Delta k_{\text{tilt}} = 0.1$ between $k_{\text{tilt}} = 0.000125t/\tau_0$

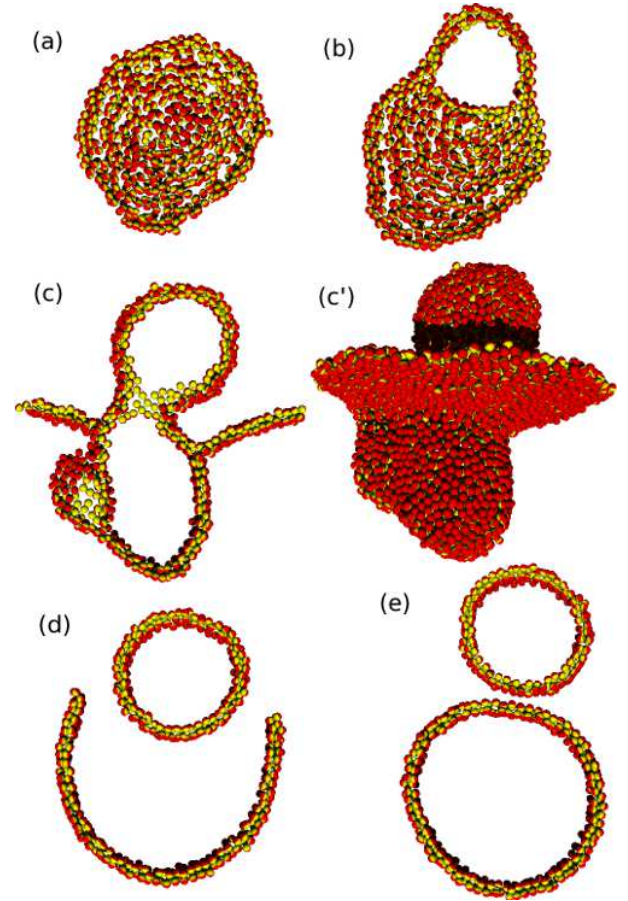


FIG. 5: (Color online) Formation of vesicles from a droplet at $N = 4000$, $\varepsilon = 2$, $\rho^* = 14$, $k_{\text{bend}} = 8$, and $C_{\text{bd}} = 0$. The tilt coefficient k_{tilt} is gradually increased as $k_{\text{tilt}} = 0.0005t/\tau_0$. Sliced snapshots are shown at (a) $t/\tau_0 = 12500$ ($k_{\text{tilt}} = 6.25$), (b) $t/\tau_0 = 13600$, (c) $t/\tau_0 = 13700$, (d) $t/\tau_0 = 14000$, and (e) $t/\tau_0 = 14500$ ($k_{\text{tilt}} = 7.25$). All molecules are also shown for $t/\tau_0 = 13700$ in (c').

and $k_{\text{tilt}} = 0.001t/\tau_0$ with $N = 500$, $\varepsilon = 2$, $\rho^* = 14$, $k_{\text{bend}} = k_{\text{tilt}}$, and $C_{\text{bd}} = 0$. The transition points are not sensitive to the path of $k_{\text{bend}}(k_{\text{tilt}})$, since the difference of the results for $k_{\text{bend}} = k_{\text{tilt}}$ and constant k_{bend} is smaller than their statistical errors.

For large aggregates with $N = 4000$, two vesicles or a vesicle with disks are formed instead of a single vesicle. Figure 5 shows an example of the formation of two vesicles. A void space is opened in the droplet, and a bilayer skirt is formed. Then, it is separated into two parts and forms two vesicles. If the separated membrane is small, a disk is formed. Since the larger droplets can have a clearer molecular layer on the surface, which prevents the shape change, higher k_{tilt} is needed to trigger the shape transition [see Fig. 6(a)]. At $N = 300$, the coexistence region of the droplets and the vesicles is narrow, since the number of the molecules is not sufficient to form the surface and inside layers. The points of the droplet-bilayer transition are also dependent on C_{bd} , while they

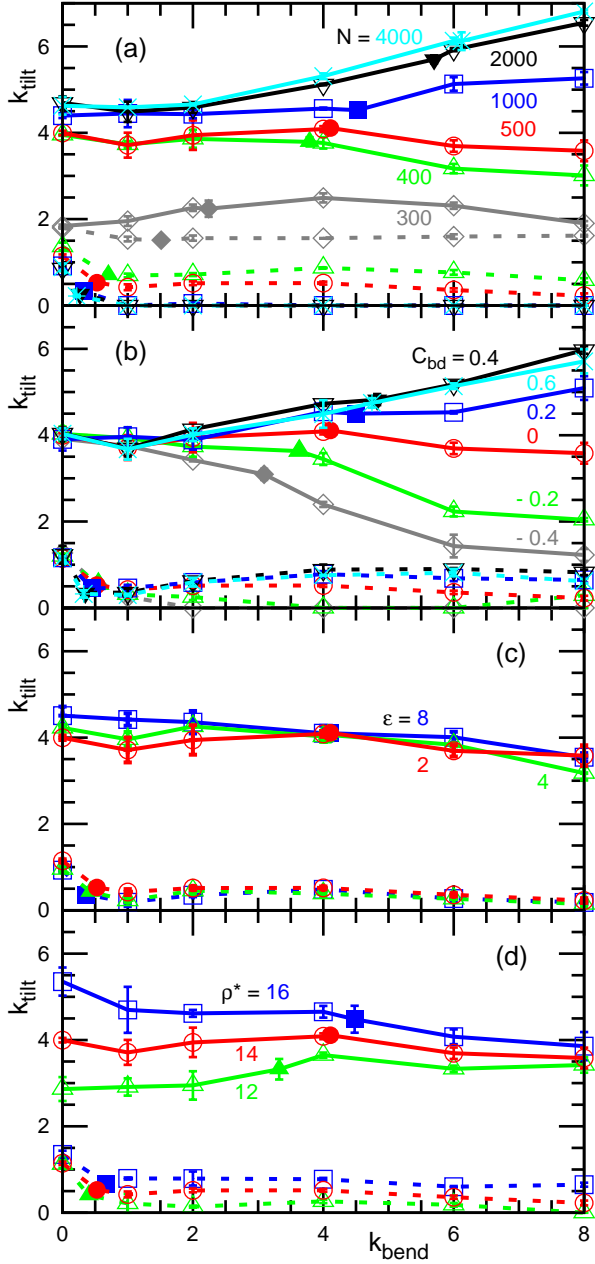


FIG. 6: (Color online) Shape transition points of molecular aggregates between the droplet and the bilayer membrane (vesicles and disks) for various (a) N , (b) C_{bd} , (c) ε , and (d) ρ^* . If not specified, $N = 500$, $\varepsilon = 2$, $\rho^* = 14$, and $C_{bd} = 0$. The solid and dashed lines represent data with increasing and decreasing k_{tilt} , respectively. The open and filled symbols represent data with fixed k_{bend} and $k_{\text{bend}} = k_{\text{tilt}}$, respectively.

are almost independent of ε and ρ^* . Thus, the bilayer stability is determined by the tilt and bending potentials but not by the attractive potential.

Let us discuss the condition required to form a stable bilayer. When all molecules have the same orientation $\mathbf{u}_i = \mathbf{u}_j$, the bending potential energy becomes zero at $C_{bd} = 0$. Thus, the bending potential with $C_{bd} = 0$

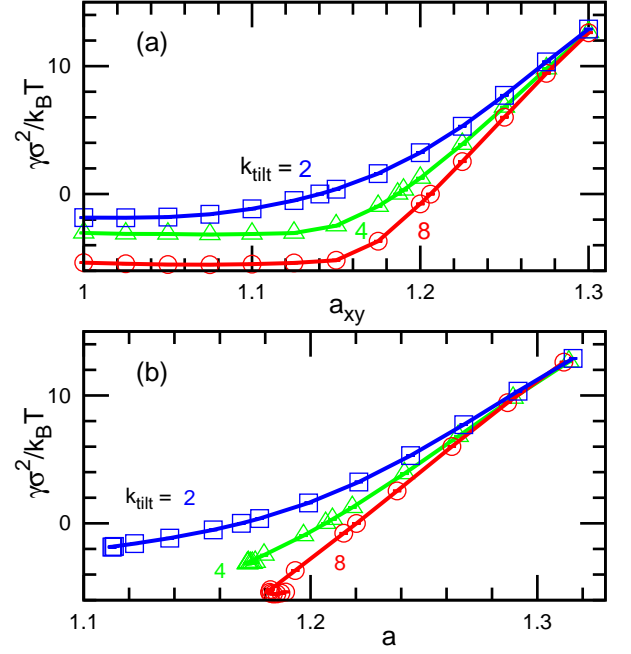


FIG. 7: (Color online) Surface tension γ of a flat membrane at $N = 512$, $\rho^* = 14$, $\varepsilon = 2$, $k_{\text{bend}} = k_{\text{tilt}}$, and $C_{bd} = 0$. Dependence of γ on (a) the projected area per molecule $a_{xy} = 2A_{xy}/N\sigma^2$ and (b) the intrinsic area per molecule $a = 2A/N\sigma^2$. The squares, triangles, and circles represent γ for $k_{\text{tilt}} = 2, 4$, and 8 , respectively. The error bars are smaller than the line thickness.

can have the minimum energy for any structure of the aggregate. Therefore, the spherical liquid droplet, which has the minimum surface area, would be the equilibrium state at $k_{\text{tilt}} = 0$ instead of the bilayer. However, large vesicles with $N \geq 1000$ and planar membranes can maintain their bilayer structure as a metastable state even at $k_{\text{tilt}} = 0$ with finite k_{bend} . Note that the capability to keep a pre-formed bilayer membrane does not guarantee the self-assembly to the bilayer. In particular, the periodic boundary condition is a strong constraint, which can keep the bilayer membrane as a thin liquid layer even at $k_{\text{tilt}} = k_{\text{bend}} = 0$. In order to obtain the spontaneous formation of the bilayer membrane, $k_{\text{tilt}} > 2$ is required.

B. Calculation of membrane properties

To investigate the membrane properties, we formed a nearly planar membrane without edges or pores. The membrane area and the surface tension are varied by increasing or decreasing the projected area $A_{xy} = L_x L_y$, where $L_x = L_y$. The membrane has a clear bilayer structure (see Fig. 2). The intrinsic area of the tensionless membrane per molecule $a_0 = 2A_0/N\sigma^2$, the area compression modulus K_A , and the half lifetime τ_{ff} of the flip-flop motion are calculated from the flat membranes with $N = 512$. The bending rigidity κ and the diffusion coef-

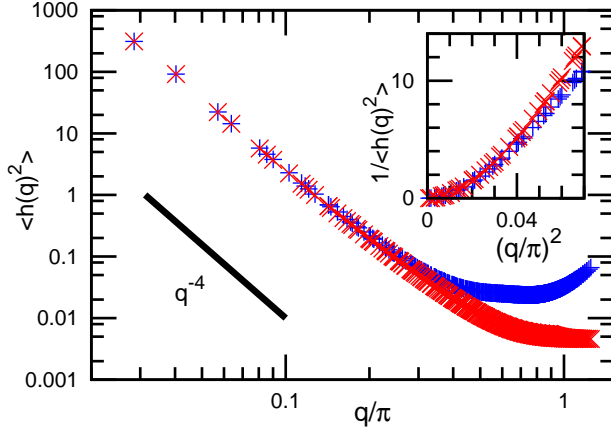


FIG. 8: (Color online) Spectra of undulation modes $\langle |h(q)|^2 \rangle$ of nearly planar, tensionless membranes ($\gamma = 0$) at $N = 8192$, $\rho^* = 14$, $\varepsilon = 2$, $k_{\text{bend}} = k_{\text{tilt}} = 8$, and $C_{\text{bd}} = 0$. Results for $\langle |h(q)|^2 \rangle$ calculated from the molecular positions (+) and from the averaged positions on a square mesh (\times) are shown. The inset shows the dependence of $1/\langle |h(q)|^2 \rangle$ on q^2 , which is used to extract the bending rigidity κ .

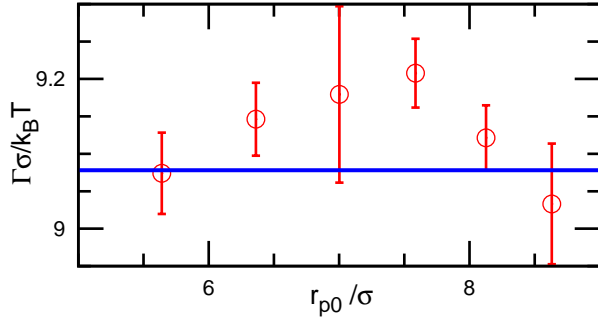


FIG. 9: (Color online) Line tension Γ of membrane edge at $\varepsilon = 2$, $\rho^* = 14$, $k_{\text{bend}} = 4$, $k_{\text{tilt}} = 4$, and $C_{\text{bd}} = 0$. The circles represent Γ calculated from a pore on the flat membrane at $N = 2048$. The solid line represents Γ calculated from the striped membrane at $N = 512$: $\Gamma\sigma/k_B T = 9.08 \pm 0.06$.

ficient D are calculated at larger tensionless membranes with $N = 8192$. The line tension Γ of membrane edge is calculated from the strip of the flat membrane with $N = 512$.

The surface tension γ is given by^{34,35}

$$\gamma = \langle P_{zz} - (P_{xx} + P_{yy})/2 \rangle L_z, \quad (13)$$

with the diagonal components of the pressure tensor

$$P_{\alpha\alpha} = (Nk_B T - \sum_i \alpha_i \frac{\partial U}{\partial \alpha_i})/V, \quad (14)$$

where $\alpha \in \{x, y, z\}$. When the potential interaction crosses the periodic boundary, the periodic image $\alpha_i + nL_\alpha$ nearest to the other interacting molecules is employed. The intrinsic area A of the membrane is larger than the projected area A_{xy} in the xy -plane due to the

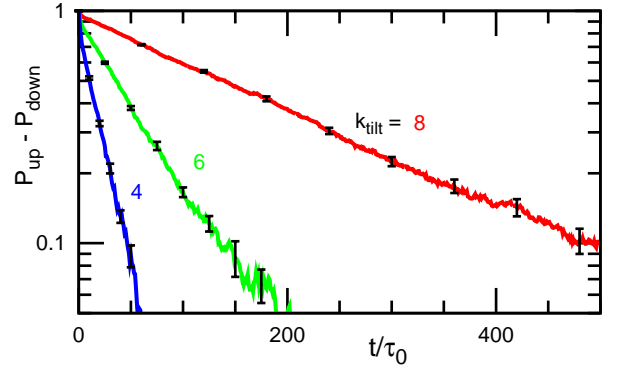


FIG. 10: (Color online) Time development of the probability difference $P_{\text{up}} - P_{\text{down}}$ of the molecules in the upper and lower monolayers at $N = 512$, $\rho^* = 14$, $\varepsilon = 2$, $k_{\text{bend}} = 0$, and $C_{\text{bd}} = 0$. At the initial states ($t = 0$), $P_{\text{up}} = 1$ and $P_{\text{down}} = 0$. The error bars are displayed at several data points.

membrane undulations. We calculate A from a $\sqrt{N/2} \times \sqrt{N/2}$ square mesh with $(x_{\text{mh}}, y_{\text{mh}}) = (d_{\text{mh}}i, d_{\text{mh}}j)$. The height z_{mh} of a mesh point is obtained from the weighted average of molecular position \mathbf{r}_i^s in the four neighbor cells, with $z_{\text{mh}} = \sum_i z_i w_{\text{mh}}(x_i, y_i) / (\sum_i w_{\text{mh}}(x_i, y_i))$ and $w_{\text{mh}}(x_i, y_i) = (1 - |x_i - x_{\text{mh}}|/d_{\text{mh}})(1 - |y_i - y_{\text{mh}}|/d_{\text{mh}})$. Figure 7 shows the area dependence on the surface tension γ . The tension γ exhibits a roughly linear increase with the molecular area at $\gamma \gtrsim 0$. The compressed membrane with $\gamma < 0$ buckles out of plane and has the larger intrinsic area A than the projected area A_{xy} . Similar γ dependence and buckling are obtained in the simulations of other molecular models^{29,36} and meshless models^{7,10}.

The area A_0 of the tensionless membrane ($\gamma = 0$) is obtained by the minimization of γ , where the projected area is updated as $A_{xy}^{\text{new}} = A_{xy} - b\bar{\gamma}\Delta t_\gamma$ every Δt_γ interval, where $\bar{\gamma}$ is the time average for Δt_γ . We use $b\tau_0 = 0.00025$ to 0.005 and $\Delta t_\gamma/\tau_0 = 50$ or 100 . The area compression modulus K_A is defined as

$$K_A = A_0 \partial\gamma / \partial A|_{A=A_0}. \quad (15)$$

We calculate K_A from the slope of a - γ lines shown in Fig. 7(b).

The bending rigidity κ is calculated from the spectra of undulation modes $\langle |h(q)|^2 \rangle$ of the planar membranes in Fourier space^{1,37,38},

$$\langle |h(q)|^2 \rangle = \frac{k_B T}{\gamma q^2 + \kappa q^4}. \quad (16)$$

Figure 8 clearly shows the q^{-4} dependence of the tensionless membrane. We calculate $|h(q)|^2$ from the raw data (the particle position \mathbf{r}_i^s), as well as from the square mesh with the same mesh-points which were used for the estimation of the intrinsic area A . Averaging over the mesh removes most of the effects of the molecular protrusions. The bending rigidity κ is estimated from a fit of $1/\langle |h(q)|^2 \rangle = (\kappa/k_B T)(q^2)^2$ for $(q/\pi)^2 < 0.015$, where

the difference of two spectra is very small (see the inset of Fig. 8).

The line tension Γ of the membrane edge is calculated from the strip of the flat membrane as^{39,40}

$$\Gamma = \langle P_{xx} - (P_{yy} + P_{zz})/2 \rangle L_y L_z / 2, \quad (17)$$

since Γ is the energy per unit length of the membrane edge, and the length of the membrane edge is $2L_x$. Since the striped membrane is tensionless, $\langle P_{yy} \rangle = \langle P_{zz} \rangle \simeq 0$ for solvent-free simulations. The tension Γ and its error bar are estimated from the average and standard deviations for $L_x/\sigma = 14, 15, 16,$ and 18 . Alternatively, Γ can be also calculated from a circular pore on the flat membrane^{7,39}. In this case, Γ is balanced with the surface tension γ as $\Gamma = \gamma r_{p0}$. Since one has to estimate the pore radius r_{p0} , this method gives larger statistical errors as shown in Fig. 9. Therefore, we used the membrane strip for the calculation of Γ .

In bilayer membranes, molecules can move laterally on a monolayer and transversely between upper and lower monolayers. The lateral diffusion coefficient D of the molecules is calculated from the diffusion of the molecular projections in the xy plane; $D = \langle (x_i(t) - x_i(0))^2 + (y_i(t) - y_i(0))^2 \rangle / 4t$. In the fluid phase, the molecules exhibit a fast diffusion rate $D/D_0 = 0.05$ to 0.1 .

The relaxation time of the transverse motion (flip-flop) between the upper and lower monolayers is measured from the relaxation of the labeled molecules^{26,41}. The differential equation of the probability $P_{\text{up}}(t)$ ($P_{\text{down}}(t)$) of the molecules, which belong to the upper (lower) monolayer, is given by $dP_{\text{up}}/dt = -k_u P_{\text{up}} + k_d P_{\text{down}}$, where $P_{\text{up}} + P_{\text{down}} = 1$. For planar membranes, $k_u = k_d$, and $P_{\text{up}} = P_{\text{down}} = 1/2$ at $t \rightarrow \infty$. When the molecules in the upper monolayer are initially labeled ($P_{\text{up}}(0) = 1$), the probability decays as

$$P_{\text{up}}(t) - P_{\text{down}}(t) = \exp[-(k_u + k_d)t] \quad (18)$$

with the half lifetime $\tau_{\text{ff}} = \ln(2)/(k_u + k_d)$. Figure 10 shows that $P_{\text{up}}(t) - P_{\text{down}}(t)$ indeed follows the exponential decay in our simulations. Either the z component of the position \mathbf{r}_i^e or orientation \mathbf{u}_i can be used to detect the monolayer, to which a molecule belongs. Both \mathbf{r}_i^e and \mathbf{u}_i give the same probability distribution (entirely same for most of the parameters), since both the quantities have a clear minimum between two peaks (see Fig. 2).

C. Parameter dependence of membrane properties

Figures 11–18 show the parameter dependence of the properties of the tensionless membrane. The bilayer membrane is formed in the fluid phase over broad ranges of the parameters due to the multibody attractive potential. A gel phase is obtained only at a large value of ρ^* in Eq. (3). The fluid-gel transition occurs at $\rho^* = 16$ and $\rho^* = 15$ for $\varepsilon = 2$ and 8 , respectively [see jumps of D in Fig. 11(e)]. As ρ^* decreases, the lateral diffusion and flip-flop motion become faster, and the membrane elasticities

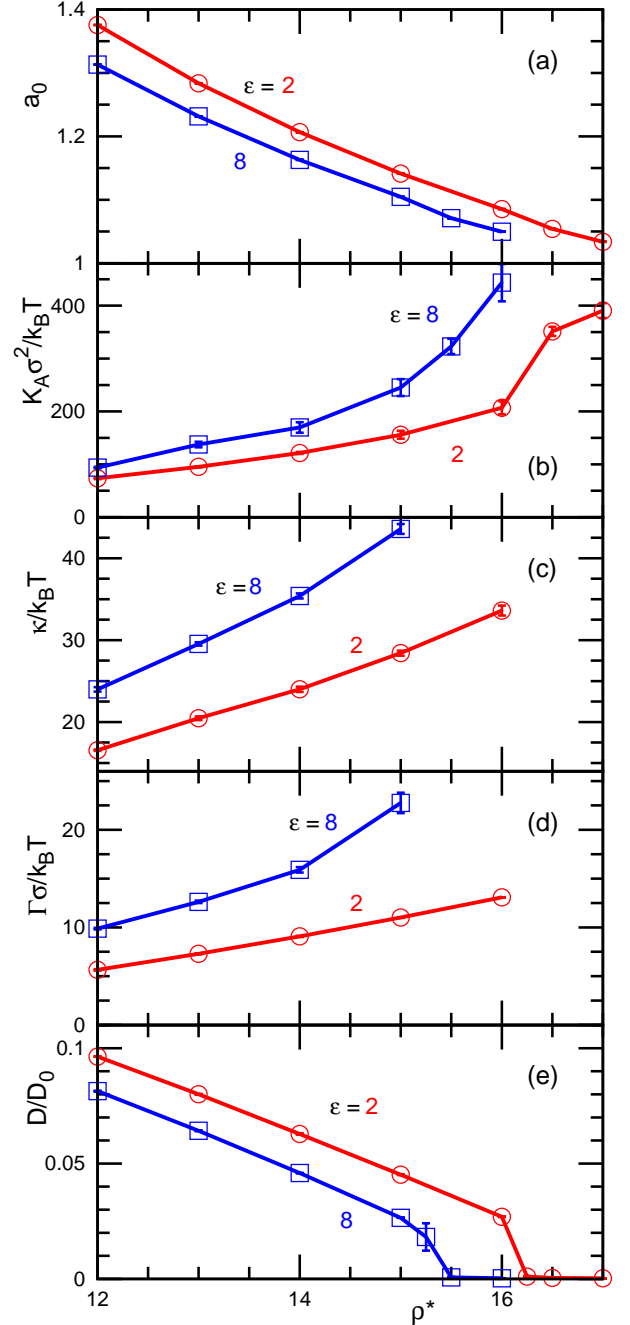


FIG. 11: (Color online) Parameter ρ^* dependence of (a) the intrinsic area $a_0 = 2A_0/N\sigma^2$ per molecule, (b) area compression modulus K_A , (c) bending rigidity κ , (d) line tension Γ , and (e) diffusion coefficient D for the tensionless membrane at $k_{\text{tilt}} = 4$, $k_{\text{bend}} = 4$, and $C_{\text{bd}} = 0$. The circles and squares represent data for $\varepsilon = 2$ and 8 , respectively.

(K_A , κ , Γ) decrease [see Figs. 11 and 18(d)]. The intrinsic area $a_0 = 2A_0/N\sigma^2$ per molecule ($N/2$ molecules in one of monolayers) decreases with increasing ρ^* and approaches the closest-packing area $\sqrt{3}\sigma^2/2 \simeq 0.87\sigma^2$ in the gel phase. In this paper, we focus on the fluid mem-

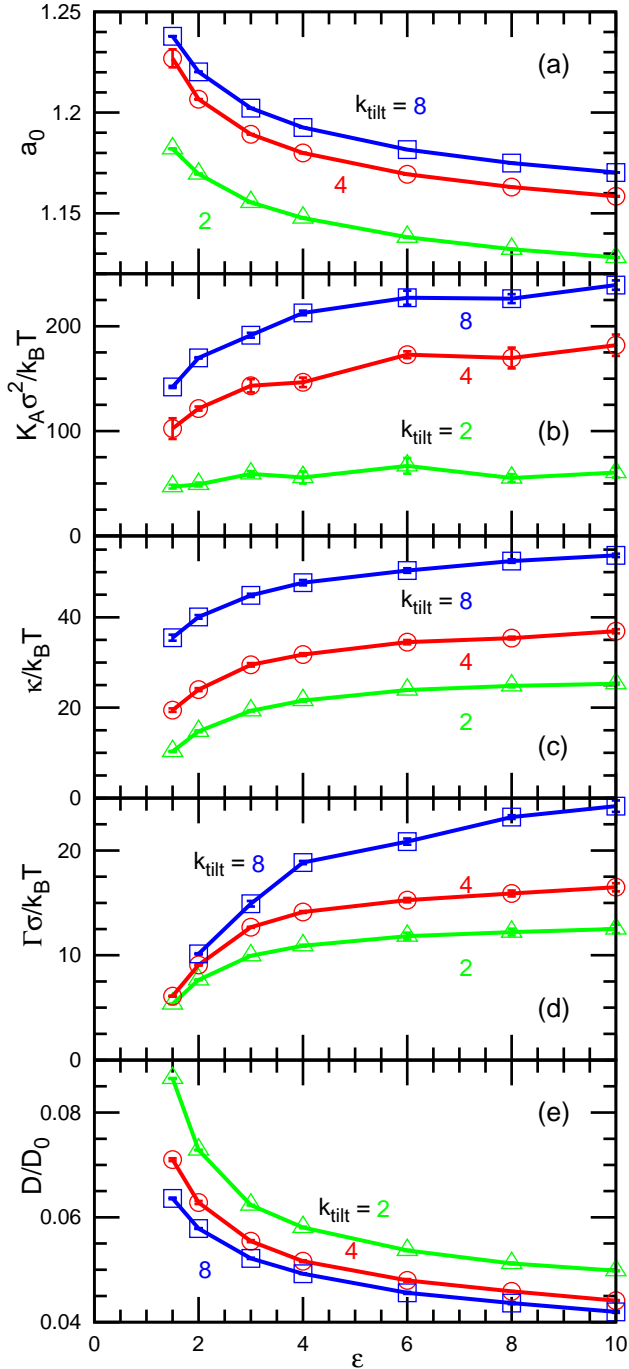


FIG. 12: (Color online) Parameter ε dependence of (a) $a_0 = 2A_0/N\sigma^2$, (b) K_A , (c) κ , (d) Γ , and (e) D for $\rho^* = 14$, $k_{\text{bend}} = k_{\text{tilt}}$, and $C_{\text{bd}} = 0$. The triangles, circles, and squares represent data for $k_{\text{tilt}} = 2, 4$, and 8 , respectively.

brane and set $\rho^* = 14$, hereafter.

The dependence on the strength of attraction ε in Eq. (1) is shown in Fig. 12. It has a tendency similar to ρ^* dependence. The line tension Γ can be varied by ε . At $\varepsilon = 1$, Γ is close to $k_B T/\sigma$ and the bilayer membrane is accompanied by free molecules (gas) with the average

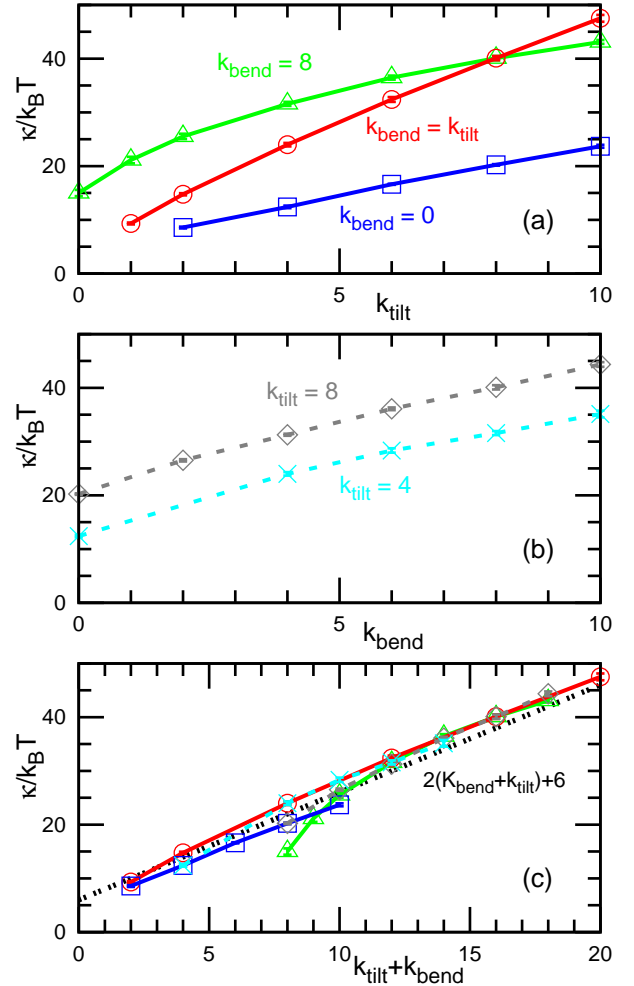


FIG. 13: (Color online) Bending rigidity κ dependence on (a) k_{tilt} , (b) k_{bend} , and (c) $k_{\text{tilt}} + k_{\text{bend}}$ for $\rho^* = 14$, $\varepsilon = 2$, and $C_{\text{bd}} = 0$. The solid lines with squares, circles, and triangles represent data for $k_{\text{bend}} = 0$, $k_{\text{bend}} = k_{\text{tilt}}$, and $k_{\text{bend}} = 8$, respectively. The dashed lines with crosses and diamonds represent data for $k_{\text{tilt}} = 4$ and 8 , respectively.

density of the gas $\sim 0.001/\sigma^3$. The molecules depart from the bilayer membrane and return. At $\varepsilon = 0.75$ with $k_{\text{bend}} = k_{\text{tilt}} = 4$ and $C_{\text{bd}} = 0$, the bilayer membrane breaks and small micelles are formed ($\simeq 60$ molecules per micelle for $N/V = 0.08/\sigma^3$). On the other hand, no free molecules are seen at $\varepsilon \geq 2$. The critical micelle concentration (CMC) of lipids is very low, and their chemical potential difference in solution and in membrane is typically more than $10k_B T$ per lipid⁴². Thus, the number of lipid molecules on vesicles is conserved in typical experiments. In order to keep the number of molecules on membrane constant during simulations, a sufficiently low CMC is required. We mainly use $\varepsilon = 2$ and 8 , where the fluid membranes without free molecules are obtained.

The bending rigidity κ of the bilayer membrane can be controlled by k_{tilt} or k_{bend} in Eq. (1). Figures 13(a) and (b) show the linear dependence of κ on k_{tilt}

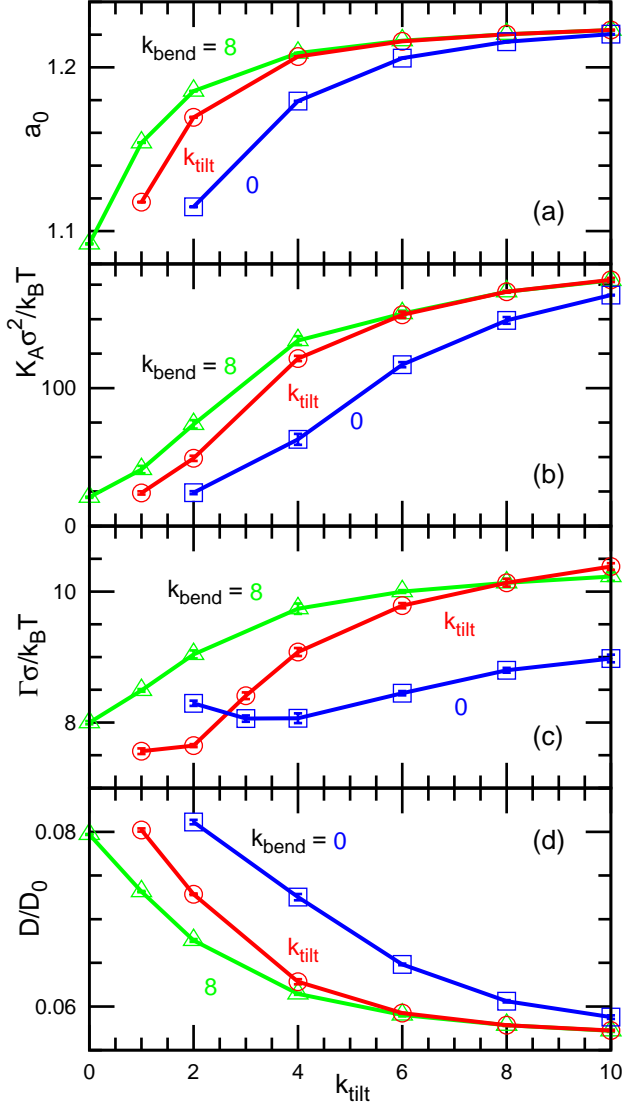


FIG. 14: Parameter k_{tilt} dependence of (a) $a_0 = 2A_0/N\sigma^2$, (b) K_A , (c) Γ , and (d) D for $\rho^* = 14$, $\varepsilon = 2$, and $C_{\text{bd}} = 0$. The squares, circles, and triangles represent data for $k_{\text{bend}} = 0$, $k_{\text{bend}} = k_{\text{tilt}}$, and $k_{\text{bend}} = 8$, respectively.

and k_{bend} , respectively. When they are plotted together for $k_{\text{tilt}} + k_{\text{bend}}$, all lines are roughly overlapped on a line $\kappa/k_B T = 2(k_{\text{tilt}} + k_{\text{bend}}) + 6$ [see Fig. 13(c)]. A large deviation from the line is seen only at one data point at $k_{\text{tilt}} = 0$ and $k_{\text{bend}} = 8$ (the leftmost triangle), where the bilayer structure is metastable. The bending rigidity κ is also weakly dependent on ε . The κ - ε curve maintains its shape and shifts upward with increasing k_{tilt} as shown in Fig. 12(c). Thus, it is expressed by $\kappa/k_B T = 2(k_{\text{tilt}} + k_{\text{bend}}) + b_\varepsilon(\varepsilon)$, where $b_\varepsilon(\varepsilon)$ is an increasing function as $b_\varepsilon(2) = 6$, $b_\varepsilon(4) = 14$, and $b_\varepsilon(8) = 18$. The area compression modulus K_A increases with increasing k_{tilt} , while K_A shows only slight dependence on k_{bend} for large k_{tilt} (see Figs. 14 and 15). The other membrane properties a , Γ , and D show weak de-

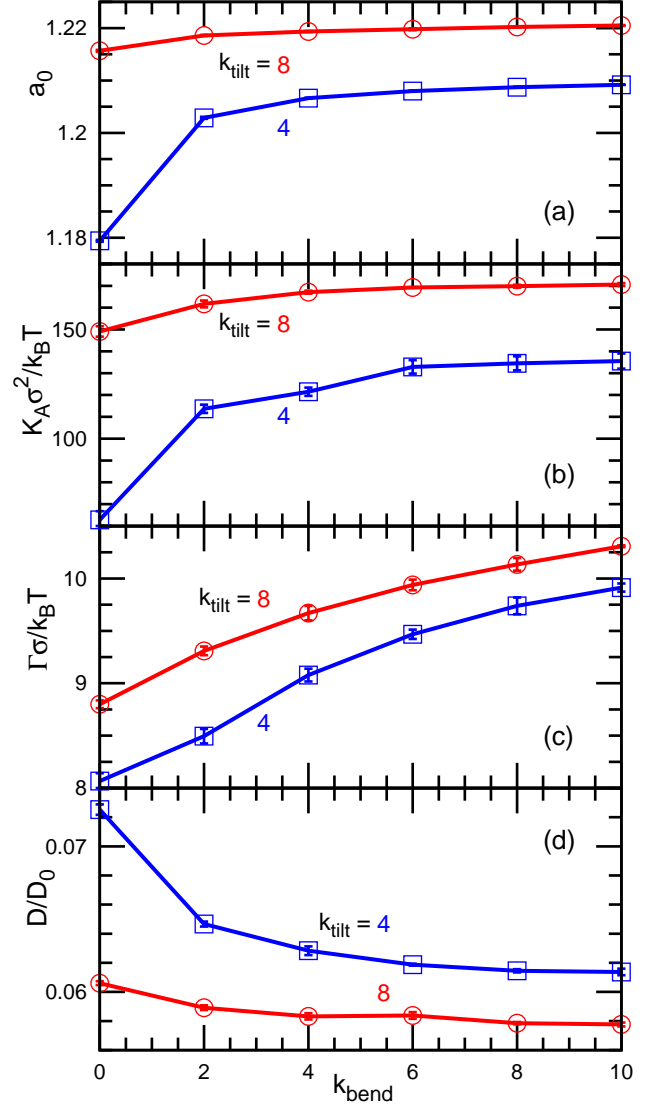


FIG. 15: (Color online) Parameter k_{bend} dependence of (a) $a_0 = 2A_0/N\sigma^2$, (b) K_A , (c) Γ , and (d) D for $\rho^* = 14$, $\varepsilon = 2$, and $C_{\text{bd}} = 0$. The squares and circles represent data for $k_{\text{tilt}} = 4$ and 8 , respectively.

pendence on k_{tilt} and k_{bend} . Thus, κ can be varied by k_{tilt} or k_{bend} without a large variation in Γ . The modulus K_A can be varied by k_{tilt} .

The bending elasticity generated by the orientation-dependent potentials can be derived from the Helfrich theory for monolayer membranes. When the orientation vectors \mathbf{u}_i are equal to the normal vectors of the monolayers without tilt deformation, the bending and tilt energies are written by

$$U_{\text{cv}} = \int dA \frac{\kappa'_{\text{bend}}}{2} [(C_1 - C'_0)^2 + (C_2 - C'_0)^2] + \frac{\kappa'_{\text{tilt}}}{2} [(C_1^2 + C_2^2)] \quad (19)$$

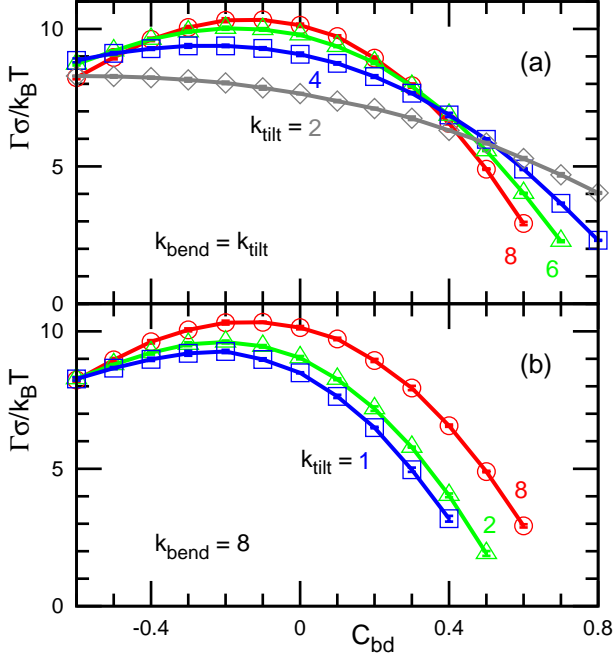


FIG. 16: (Color online) Line tension Γ dependence on C_{bd} for (a) $k_{bend} = k_{tilt}$ and (b) $k_{bend} = 8$ at $\rho^* = 14$ and $\varepsilon = 2$. (a) The diamonds, squares, triangles, and circles represent data for $k_{tilt} = 2, 4, 6,$ and 8 , respectively. (b) The squares, triangles, and circles represent data for $k_{tilt} = 1, 2,$ and 8 , respectively.

$$= \int dA \frac{\kappa'_{bend} + \kappa'_{tilt}}{2} [(C_1 + C_2 - C_0)^2 - (\kappa'_{bend} + \kappa'_{tilt})C_1C_2 + U_0] \quad (20)$$

in the continuum limit, where C_1 and C_2 are two principal curvatures of the monolayer. The first and second terms in Eq. (19) are the contributions of the bending and tilt potentials, respectively. The spontaneous curvature of the bending potential is given by $C'_0 = C_{bd}/\bar{r}_{nb}$.²⁷ The nearest-neighbor distance $\bar{r}_{nb} \simeq 1.05\sigma$ is obtained from the radial distribution function. By assuming the hexagonal packing of the molecules in the monolayers, the monolayer bending rigidities generated by the bending and tilt potentials are estimated as $\kappa'_{bend}/k_B T = \sqrt{3}k_{bend}w_{cv}(\bar{r}_{nb})$ and $\kappa'_{tilt}/k_B T = \sqrt{3}k_{tilt}w_{cv}(\bar{r}_{nb})/2$, respectively. The bending rigidity of the monolayer is given by the sum of these $\kappa_{mono} = \kappa'_{bend} + \kappa'_{tilt}$. For the monolayer membrane, Eq. (20) gives the saddle-splay modulus $\bar{\kappa}_{mono} = -\kappa_{mono}$ and the spontaneous curvature $C_0 = \{\kappa'_{bend}/(\kappa'_{bend} + \kappa'_{tilt})\}C_{bd}/\bar{r}_{nb}$ with $U_0 = (\kappa'_{bend} + \kappa'_{tilt})(1/2 + \kappa'_{tilt}/\kappa'_{bend})C_0^2$. Thus, the bending rigidity κ of the bilayer is estimated as $\kappa = 2\kappa_{mono} \simeq (2.1k_{bend} + 1.1k_{tilt})k_B T$ from $w_{cv}(1.05\sigma) = 0.61$. This estimation of κ supports the linear dependence of the obtained simulation results on k_{bend} and k_{tilt} . The prefactor ($\simeq 2$) of k_{bend} gives the quantitative agreement, whereas the prefactor of k_{tilt} is half of the numerical estimation. In the simulation, the thermal fluctuations in-

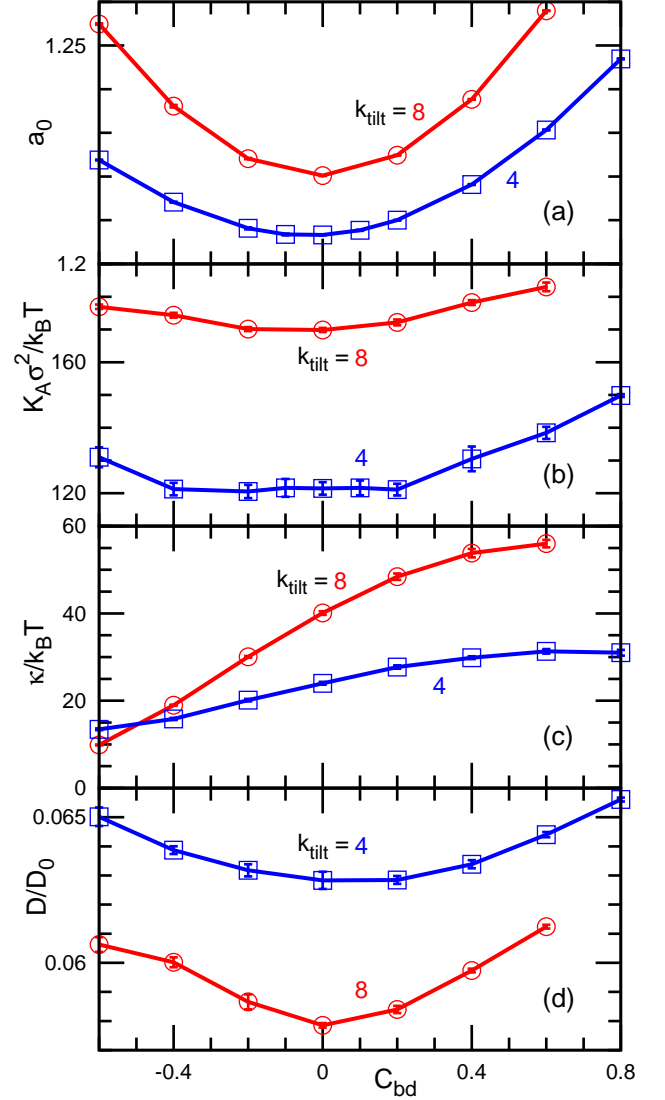


FIG. 17: (Color online) Parameter C_{bd} dependence of (a) $a_0 = 2A_0/N\sigma^2$, (b) K_A , (c) κ , and (d) D for $\rho^* = 14$, $\varepsilon = 2$, and $k_{bend} = k_{tilt}$. The squares and circles represent data for $k_{tilt} = 4$ and 8 , respectively.

duce molecular protrusion and tilt. These tilt fluctuations likely change the prefactor of k_{tilt} to twice its value ($\kappa'_{tilt}/\kappa'_{bend} = k_{tilt}/k_{bend}$). The attractive potential also adds a small bending resistance, $b_\varepsilon(\varepsilon)$.

The flip-flop time τ_{ff} shows exponential dependence on the parameters of the tilt and bending potentials, while it has weak dependence on ε (see Fig. 18). The free-energy barrier between two monolayers would be the main factor to determine τ_{ff} . It can be roughly estimated from the probability distribution of the molecular orientation as $F_{ff} = k_B T (\ln[P(u_z = 1)] - \ln[P(u_z = 0)])$ [see Fig. 2(b)]. The dashed lines in Fig. 18(a) represent F_{ff} calculated by this method. It gives very good agreements with $\ln(\tau_{ff}/\tau_0)$, and thus, the flip-flop time is written by $\tau_{ff}/\tau_0 = b_{ff} \exp(F_{ff}/k_B T)$ with $b_{ff} \simeq 1$. The barrier F_{ff} is

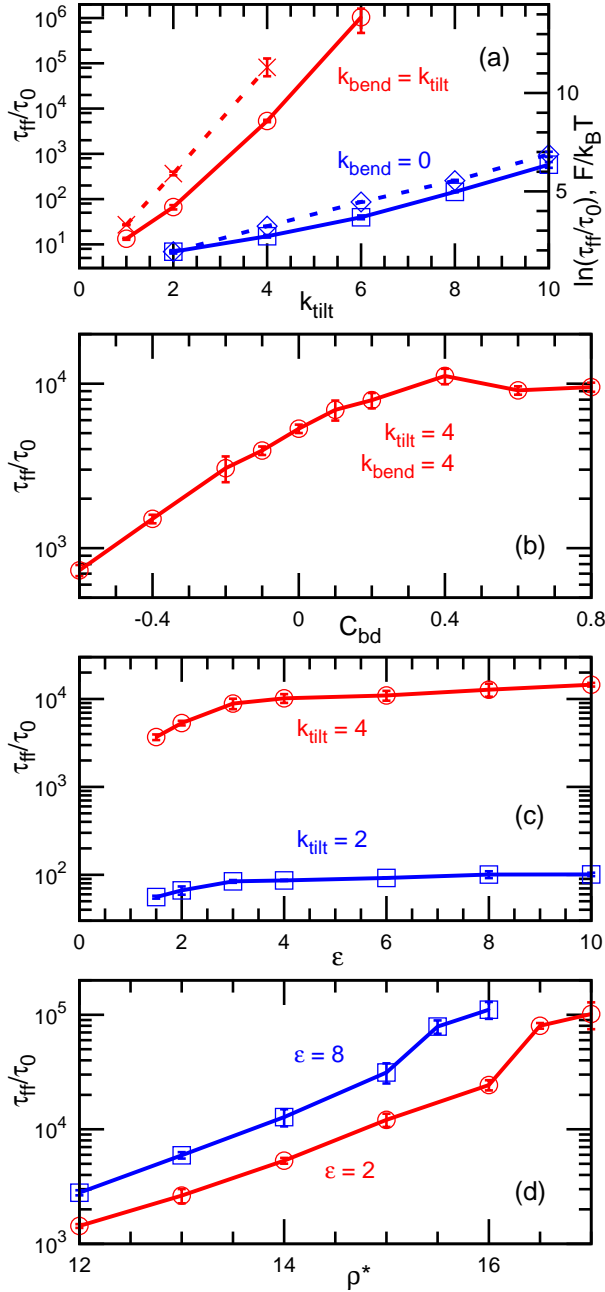


FIG. 18: (Color online) Half lifetime τ_{ff} of flip-flop motion. (a) Dependence on k_{tilt} at $\rho^* = 14$, $\epsilon = 2$, and $C_{bd} = 0$. The dashed lines represent the free-energy barrier $F_{ff}/k_B T$ estimated by the orientation distribution shown in Fig. 2(b). (b) Dependence on C_{bd} at $\rho^* = 14$ and $\epsilon = 2$. (c) Dependence on ϵ at $\rho^* = 14$, $k_{bend} = k_{tilt}$, and $C_{bd} = 0$. (d) Dependence on ρ^* at $k_{bend} = k_{tilt} = 4$ and $C_{bd} = 0$.

linear with the orientation-dependent potentials, while it is almost independent of the attractive potentials. The flip-flop rate can be tuned by k_{tilt} or k_{bend} . In typical experimental conditions, the flip-flop motion of phospholipids is very slow, and τ_{ff} is several hours or days⁴¹. At a sufficiently high k_{tilt} or k_{bend} , no flip-flop occurs in

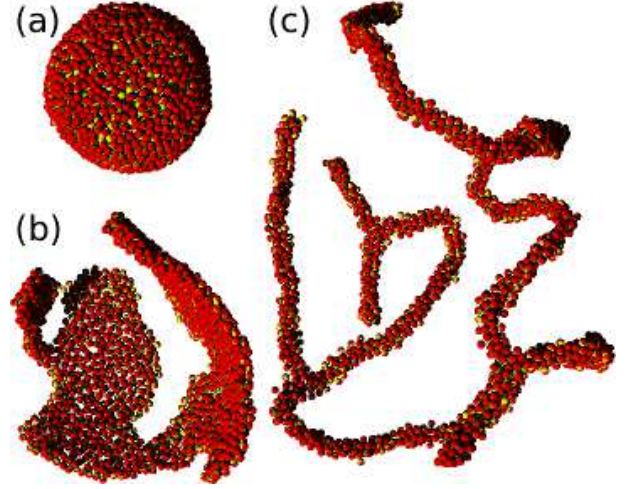


FIG. 19: (Color online) Sequential snapshots of vesicle rupture at $N = 2000$, $\epsilon = 2$, $\rho^* = 14$, $k_{bend} = 8$, $k_{tilt} = 8$, and $C_{bd} = 0.85$. (a) $t/\tau_0 = 500$. (b) $t/\tau_0 = 640$. (c) $t/\tau_0 = 3000$.

typical simulation time scales. This result agrees with the experimental observations. On the other hand, at small k_{tilt} and k_{bend} , the molecule shows very fast flip-flop, which is advantageous to equilibrate the membrane system quickly during simulations. In the present model, one can choose slow or fast flip-flop condition to match one's simulation purpose.

The spontaneous curvature of the monolayer is varied by the parameter C_{bd} . According to the above continuous theory, $C_0 = \{k_{bend}/\sigma(k_{bend} + k_{tilt})\}C_{bd}$. At high spontaneous curvature $C_0 \sim 1/\sigma$, a worm-like micelle is stabilized. As C_{bd} increases, the line tension Γ decreases, and the bilayer structure becomes unstable at $\Gamma \sim k_B T/\sigma$. The C_{bd} - Γ curves in Fig. 16 have a parabolic shape with a maximum at $C_{bd} \sim -0.1$. The bending rigidity κ and the flip-flop time τ_{ff} increase with C_{bd} , while a_0 , K_A , and D do not depend significantly on C_{bd} [see Figs. 17 and 18(b)]. At negative C_0 , the molecules easily stay at the middle of the bilayer structure (low F_{ff}), and the less clear bilayer would generate lower κ .

Membrane rupture is observed when C_{bd} is increased. Figure 19 shows the rupture process of a vesicle at $C_{bd} = 0.85$. The initial vesicle is metastable and maintains its shape for $500\tau_0$. Then, a pore opens and grows to cracks [see Fig. 19(b)]. Finally, a branched worm-like micelle is formed [see Fig. 19(c)]. Thus, the line tension and the stable structure can be varied by C_{bd} .

IV. SUMMARY

We have proposed a simple molecular model of bilayer membranes. The molecule has five degrees of freedom, three translational degrees and two orientational degrees. Since this molecular model consists of one spherical par-

ticle for the excluded volume, it is smaller than previous molecular models. Thus, this model is more efficient for large-scale simulations. Despite the extreme simplification, this model reproduces many aspects of lipid bilayer membranes.

In the present model, the properties of the fluid membranes can be controlled in broad ranges including metastable bilayer membranes. The bending rigidity κ is linearly dependent on k_{tilt} and k_{bend} . The line tension Γ of the membrane edge can be varied by ε and C_{bd} . The membrane has a wide range of fluid phase, and the fluid-gel transition point can be controlled by ρ^* . The area compression modulus K_A can be varied by k_{tilt} . The flip-flop time τ_{ff} can be varied by k_{tilt} and k_{bend} .

The corresponding time and length scales can be mapped by the membrane thickness 5nm and the lateral diffusion coefficient $\sim 10^{-8}\text{cm}^2/\text{s}$ for phospholipids⁴³. Thus, the unit length and times are estimated as $\sigma = 2$ nm and $\tau_0 \sim 0.1\mu\text{s}$, respectively.

Our model is suitable to study the details of topological-change processes of the membrane, such as molecular self-assembly, pore formation, membrane fusion, and membrane fission. Although meshless membrane models can also be used, they cannot treat detailed structures such as the fusion intermediates^{14,15}. Recently, fusion dynamics have been investigated by molecular simulations^{44–51}. However, the condition to determine the fusion pathways has not been clarified so far.

The ability to vary the membrane properties in wide ranges would be an advantage of this model for quantitative investigation of the membrane fusion pathways. On the other hand, this model is not suitable for application to phenomena, in which the stretching of hydrophobic chains or atomistic details play an important role, e.g., in the interactions of membrane proteins via hydrophobic mismatch, where molecular stretching is not negligible^{52–55}.

In this paper, we used Brownian dynamics but one can also use the Monte Carlo method and molecular dynamics with another thermostat. When the solvent-free molecular model is combined with a particle-based hydrodynamics method, multi-particle collision dynamics (MPC)^{56,57}, the hydrodynamic interaction can be taken into account as demonstrated for a meshless membrane model⁸. Thus, the present coarse-grained molecular model is efficient for large-scale dynamics of a biomembrane with or without hydrodynamic interactions and is applicable to many kinds of phenomena.

Acknowledgments

This work is supported by KAKENHI (21740308) from the Ministry of Education, Culture, Sports, Science, and Technology of Japan.

* noguchi@issp.u-tokyo.ac.jp

¹ S. A. Safran, *Statistical Thermodynamics of Surfaces, Interfaces, and Membranes* (Addison-Wesley, Reading, MA, 1994).

² R. Lipowsky and E. Sackmann, eds., *Structure and Dynamics of Membranes* (Elsevier Science, Amsterdam, 1995).

³ U. Seifert, *Adv. Phys.* **46**, 13 (1997).

⁴ G. Gompper and D. M. Kroll, in *Statistical Mechanics of Membranes and Surfaces*, edited by D. R. Nelson, T. Piran, and S. Weinberg (World Scientific, Singapore, 2004), 2nd ed.

⁵ G. Gompper and D. M. Kroll, *J. Phys. Condens. Matter* **9**, 8795 (1997).

⁶ J. M. Drouffe, A. C. Maggs, and S. Leibler, *Science* **254**, 1353 (1991).

⁷ H. Noguchi and G. Gompper, *Phys. Rev. E* **73**, 021903 (2006).

⁸ H. Noguchi and G. Gompper, *J. Chem. Phys.* **125**, 164908 (2006).

⁹ M. G. Del Pópolo and P. Ballone, *J. Chem. Phys.* **128**, 024705 (2008).

¹⁰ T. Kohyama, *Physica A* **388**, 3334 (2009).

¹¹ P. Liu, J. Li, and Y. W. Zhang, *Appl. Phys. Lett.* **95**, 143104 (2009).

¹² R. M. Fuchsli, T. Maeke, and J. S. McCaskill, *Eur. Phys. J. E* **29**, 431 (2009).

¹³ H. Yuan, C. Huang, J. Li, G. Lykotraftis, and S. Zhang, *Phys. Rev. E* **82**, 011905 (2010).

¹⁴ R. Jahn and H. Grubmüller, *Curr. Opin. Cell Biol.* **14**, 488 (2002).

¹⁵ L. V. Chernomordik and M. M. Kozlov, *Nat. Struct. Mol. Biol.* **15**, 675 (2008).

¹⁶ M. Müller, K. Katsov, and M. Schick, *Phys. Rep.* **434**, 113 (2006).

¹⁷ M. Venturoli, M. M. Sperotto, M. Kranenburg, and B. Smit, *Phys. Rep.* **437**, 1 (2006).

¹⁸ M. L. Klein and W. Shinoda, *Science* **321**, 798 (2008).

¹⁹ H. Noguchi, *J. Phys. Soc. Jpn.* **78**, 041007 (2009).

²⁰ S. J. Marrink, A. H. de Vries, and D. P. Tieleman, *Biochim. Biophys. Acta* **1788**, 149 (2009).

²¹ S. J. Marrink, A. H. de Vries, and A. E. Mark, *J. Phys. Chem. B* **108**, 750 (2004).

²² S. Izvekov and G. A. Voth, *J. Phys. Chem. B* **109**, 2469 (2005).

²³ A. Arkhipov, Y. Yin, and K. Schulten, *Biophys. J.* **95**, 2806 (2008).

²⁴ W. Shinoda, R. DeVane, and M. L. Klein, *Soft Matter* **4**, 2454 (2008).

²⁵ Z. J. Wang and M. Deserno, *J. Phys. Chem. B* **114**, 11207 (2010).

²⁶ H. Noguchi and M. Takasu, *Phys. Rev. E* **64**, 041913 (2001).

²⁷ H. Noguchi, *Phys. Rev. E* **67**, 041901 (2003).

²⁸ G. Brannigan, L. C. L. Lin, and F. L. H. Brown, *Eur. Biophys. J.* **35**, 104 (2006).

²⁹ M. Deserno, *Macromol. Rapid. Commun.* **30**, 752 (2009).

³⁰ O. Farago and N. Grønbech-Jensen, *J. Am. Chem. Soc.*

- 131**, 2875 (2009).
- ³¹ S. Takada, Z. Luthey-Schulten, and P. G. Wolynes, *J. Chem. Phys.* **110**, 11616 (1999).
- ³² M. Hamm and M. M. Kozlov, *Eur. Phys. J. B* **6**, 519 (1998).
- ³³ M. Hamm and M. M. Kozlov, *Eur. Phys. J. E* **3**, 323 (2000).
- ³⁴ M. P. Allen and D. J. Tildesley, *Computer simulation of liquids* (Clarendon Press, Oxford, 1987).
- ³⁵ J. S. Rowlinson and B. Widom, *Molecular Theory of Capillarity* (Clarendon, Oxford, 1982).
- ³⁶ W. K. den Otter, *J. Chem. Phys.* **123**, 214906 (2005).
- ³⁷ R. Goetz, G. Gompper, and R. Lipowsky, *Phys. Rev. Lett.* **82**, 221 (1999).
- ³⁸ E. Lindahl and O. Edholm, *Biophys. J.* **79**, 426 (2000).
- ³⁹ T. V. Tolpekina, W. K. den Otter, and W. J. Briels, *J. Chem. Phys.* **121**, 8014 (2004).
- ⁴⁰ B. J. Reynwar and M. Deserno, *Bioinerphases* **3**, FA117 (2008).
- ⁴¹ R. D. Kornberg and H. M. McConnell, *Biochemistry* **10**, 1111 (1971).
- ⁴² C. Tanford, *The hydrophobic effect: formation of micelles and biological membranes* (Wiley, New York, 1980).
- ⁴³ E. S. Wu, K. Jacobson, and D. Papahadjopoulos, *Biochemistry* **16**, 3936 (1977).
- ⁴⁴ H. Noguchi and M. Takasu, *J. Chem. Phys.* **115**, 9547 (2001).
- ⁴⁵ H. Noguchi and M. Takasu, *Biophys. J.* **83**, 299 (2002).
- ⁴⁶ H. Noguchi, *J. Chem. Phys.* **117**, 8130 (2002).
- ⁴⁷ M. Müller, K. Katsov, and M. Schick, *J. Chem. Phys.* **116**, 2342 (2002).
- ⁴⁸ D. W. Li and X. Y. Liu, *J. Chem. Phys.* **122**, 174909 (2005).
- ⁴⁹ J. Shillcock and R. Lipowsky, *Nat. Mater.* **4**, 225 (2005).
- ⁵⁰ A. F. Smeijers, A. J. Markvoort, K. Pieterse, and P. A. J. Hilbers, *J. Phys. Chem. B* **110**, 13212 (2006).
- ⁵¹ V. Knecht and S. J. Marrink, *Biophys. J.* **92**, 4254 (2007).
- ⁵² R. Phillips, T. Ursell, P. Wiggins, and P. Sens, *Nature* **459**, 379 (2009).
- ⁵³ J. B. Fournier, *Eur. Phys. J. B* **11**, 261 (1999).
- ⁵⁴ F. J. de Meyer, M. Venturoli, and B. Smit, *Biophys. J.* **95**, 1851 (2008).
- ⁵⁵ B. West, F. L. H. Brown, and F. Schmid, *Biophys. J.* **96**, 101 (2009).
- ⁵⁶ R. Kapral, *Adv. Chem. Phys.* **140**, 89 (2008).
- ⁵⁷ G. Gompper, T. Ihle, D. M. Kroll, and R. G. Winkler, *Adv. Polym. Sci.* **221**, 1 (2009).